CCFE-PR(17)42

P. Manas, Y. Camenen, S. Benkadda, H. Weisen, C. Angioni, F.J. Casson, C. Giroud, M. Gelfusa, M. Maslov and JET contributors

Gyrokinetic modelling of impurity peaking in JET H-mode plasmas

Gyrokinetic modelling of impurity peaking in JET H-mode plasmas

P. Manas[1;2], Y. Camenen[2], S. Benkadda[2], H. Weisen[3], C. Angioni[1], F.J. Casson[4], C. Giroud[4], M. Gelfusa[5], M. Maslov[4] and JET contributors

[1] Max-Planck-Institut für Plasmaphysik, D-85748 Garching, Germany
[2] Aix-Marseille Université, CNRS, PIIM UMR7345, 13397 Marseille, France
[3] Ecole Polytechnique Fédérale de Lausanne (EPFL), Swiss Plasma Center (SPC), CH-1015 Lausanne, Switzerland
[4] CCFE, Culham Science Centre, Abingdon, OX14 3DB, UK
[5] Department of Industrial Engineering, University of Rome "Tor Vergata", via del Politecnici 1, Roma, Italy

Gyrokinetic modelling of impurity peaking in JET H-mode plasmas

P. Manas[1,2], Y. Camenen[2], S. Benkadda[2], H. Weisen[3], C. Angioni[1], F. J. Casson[4], C. Giroud[4], M. Gelfusa[5], M. Maslov[4] and JET contributors*

[1] *Max-Planck-Institut für Plasmaphysik, D-85748 Garching, Germany*

[2] *Aix-Marseille Université, CNRS, PIIM UMR7345, 13397 Marseille, France*

[3] *Ecole Polytechnique Fédérale de Lausanne (EPFL), Swiss Plasma Center (SPC), CH-1015 Lausanne, Switzerland*

[4] *CCFE, Culham Science Centre, Abingdon, OX14 3DB, UK*

[5] *Department of Industrial Engineering, University of Rome "Tor Vergata", via del Politecnici 1, Roma, Italy*

* *See the Appendix of F. Romanelli et al., Proceedings of the* 25^{th} *IAEA Fusion Energy Conference 2014, Saint Petersburg, Russia*

Quantitative comparisons are presented between gyrokinetic simulations and experimental values of the carbon impurity peaking factor in a database of JET H-modes during the carbon wall era. These plasmas feature strong NBI heating, hence high values of toroidal rotation and correponding gradient. Furthermore, the carbon profiles present particularly interesting shapes for fusion devices, i.e. hollow in the core and peaked near the edge. Dependencies of the experimental carbon peaking factor (R/L_{n_C}) on plasma parameters are investigated via multilinear regressions. A marked correlation between R/L_{n_C} and the normalised toroidal rotation gradient is observed in the core, which suggests an important role of the rotation in establishing hollow carbon profiles. The carbon peaking factor is then computed with the gyrokinetic code GKW, using a quasi-linear approach, supported by few non-linear simulations. The comparison of the quasi-linear predictions to the experimental values at mid-radius reveals two main regimes. At low normalised collisionality, ν_*, and $T_e/T_i < 1$ the gyrokinetic simulations quantitatively recover experimental carbon density profiles, provided roto-diffusion is taken into account. In contrast, at higher ν_* and $T_e/T_i > 1$, the very hollow experimental carbon density profiles are never predicted by the simulations and the carbon density peaking is systematically over estimated. This points at a possible missing ingredient in this regime.

Keywords:

I. INTRODUCTION

Understanding impurity transport in the core of tokamak plasmas is central to achieving controlled fusion. Indeed impurities are ubiquitous in these devices and their presence in the core are detrimental to plasma confinement (fuel dilution, Bremsstrahlung). Thus, impurity transport modelling is a crucial topic widely adressed in the literature (e.g. [1] and references therein). Combined neoclassical and gyrokinetic simulations have come to a point where quantitative comparisons with experimental observations can be performed for light [2–11] and heavy impurities [12, 13].

In this context, a database of NBI heated H-mode JET plasmas (during the carbon wall era) which has been used for particle and momentum transport studies [14–16], has been extended to also include intrinsic carbon impurity density profiles and is scrutinised with an emphasis on carbon transport. This database is particularly interesting for quantitative comparisons with numerical simulations as it mainly consists of flat/hollow core impurity profiles (attractive with respect to impurity accumulation) and strong normalised toroidal rotation and ion temperature gradients which suggests strong convections via thermo-diffusion [17] and roto-diffusion [18]. The latter is a relatively new mechanism and has been found experimentally relevant for light impurities modelling in [2, 3]. Thus, it could play a non negligible role in the NBI heated JET discharges of this study.

Modelling of the neoclassical and turbulent transport are performed with the neoclassical code NEO [19] and the gyrokinetic code GKW [20] respectively. In this study, a statistical approach is adopted, i.e. considering a large number of discharges and spanning a wide plasma parameter space. To achieve a large number of simulations at a reasonable computational cost, a quasi-linear approach is adopted. For a few cases, non-linear simulations are performed to validate the quasi-linear model. The objectives of this study are twofold: characterise the main experimental correlations between the carbon peaking factor and the plasmas parameters and perform quantitative comparisons between theoretical and experimental carbon peaking factors to assess the impact of roto-diffusion in the development of these carbon hollow profiles.

The paper is organised as follows. In section II, the database of JET H-modes is described. Multilinear regressions are performed and the dependencies of the carbon peaking factor on the plasma parameters are underlined. In section III, the method applied to compute R/L_{n_C} from neoclassical and gyrokinetic simulations is described in details. Finally, in section IV, results from these simulations are compared to experimental values of R/L_{n_C} and conclusions are drawn.

II. EXPERIMENTAL JET DATABASE

A. Plasma parameters and profiles

The database used in this study consists of ~ 156 stationary state phases of deuterium plasmas with improved magnetic equilibrium reconstruction (computed using experimental measurements to constrain the current density profile in EFIT [21]). These plasmas are dominantly heated by Neutral Beam Injection (8 to 22 MW) and in some cases by Ion Cyclotron Resonance Heating (0 to 6MW). The database was used in previous studies to characterise non-diffusive momentum transport and particle peaking dependencies [14–16] and has been extended to include carbon profiles. In the present study, emphasis is then given to the carbon transport. A wide range of plasma parameters is covered: plasma current $I_p = 1 - 2.6$ MA, safety factor at 95% of the poloidal magnetic flux $q_{95} = 2.4 - 6$, central electron density $n_e = 2.6{-}7.6{\times}10^{19}$ m^{-3}, toroidal magnetic field strength $B_T = 1.35 - 3.4$ T and central deuterium Mach number $M_D = 0.14 - 0.38$. The electron density and temperature are measued via Thomson scattering. The carbon density, temperature and toroidal rotation are measured via Charge Exchange Recombination Spectroscopy [22] on the C^{5+} $N = 8$ to 7 line at 529.1 nm.

In Fig. 1, typical profiles of the carbon density, ion temperature and angular toroidal frequency are shown together with their corresponding normalised gradients $R/L_x = -R/x(\partial x/\partial r)$ with R the major radius, r the minor radius and x the considered quantity. The normalised gradients and their respective error bars (essential for meaningful comparisons with gradient driven simulation results) are computed following the same methodology as in Appendix A of [23]. The carbon profile is hollow in the core and peaked close to the edge of the plasma. These profiles are typical of the database and their nature (no impurity accumulation in the core) gives strong incentive for quantitative modelling. Due to the high level of NBI in these discharges, the normalised toroidal rotation gradient, u', and ion temperature gradient, R/L_{T_i}, are rather high, which motivates to investigate the role of the associated impurity convection mechanisms in the sustainment of hollow impurity profiles.

We note that intermittent transport processes can affect the plasma profiles from $r/a = 0$ to $r/a = 0.2$ for sawteeth and from $r/a = 0.8$ to $r/a = 1$ for edge localised modes (ELMs). The modelling, which does not include these transient mechanisms is, therefore, restricted to r/a=0.55. For two particular cases in section IV the analysis is extended to a wider radial range,$0.45 < r/a < 0.85$.

B. Multilinear regressions of the carbon peaking factor

Before addressing numerical simulations and comparisons with the experiment, multilinear regressions are performed on the database to identify the plasma parameters on which the carbon peaking factor R/L_{n_C} depends.

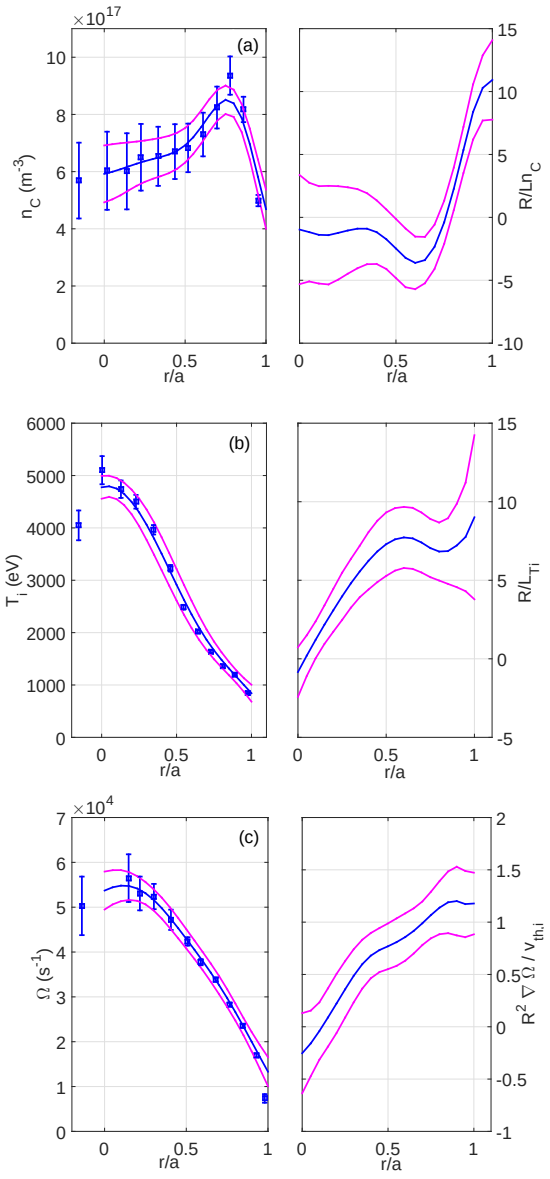

FIG. 1: Mean profiles (blue lines) of carbon density (a), temperature (b) and angular velocity (c) together with their corresponding normalised gradients (right pannels). Standard deviations (magenta lines) and experimental measurements (blue squares) are also represented.

Correlations are unavoidable and need to be kept in mind when considering multilinear regressions. The degree of correlation between the experimental parameters is assessed in Appendix A where a correlation coefficient is computed for the following set of variables: $u' = R^2/v_{th,i}\partial\Omega/\partial r$, R/L_n, R/L_{T_i}, R/L_{T_e}, the ratio of the total plasma pressure to magnetic pressure β, $\rho_* = \rho_i/a$ with ρ_i the ion Larmor radius, a the plasma minor radius at the last closed flux surface, the local safety factor q, the magnetic shear $\hat{s}$, the normalised collisionality $\nu_* = \nu_{ei}q/\epsilon^{3/2}$, T_e/T_i, M_D and R/L_{n_C}.

Several plasma parameters appear to be strongly correlated, with a correlation coefficient $r_c > 0.2$ in the table.

We note three important correlations. The correlation between ν_* and R/L_n which has been largely documented in the literature (e.g. [14, 25]) and is a result of the collisionality dependence of particle transport. The correlation between ν_* and T_e/T_i and finally between R/L_{T_i} and u' which is expected in NBI heated plasmas. From the correlation table, it already appears that one cannot directly disentangle the impurity peaking associated to a convection driven by R/L_{T_i} or u' from regressions only.

Another point of interest are of course the correlations between R/L_{n_C} and the other parameters. Though r_c values are relatively small (< 0.2), i.e. R/L_{n_C} values are scattered with respect to the linear fits, the dominant linear correlations are with R/L_n, $\hat{s}$, ν_*, T_e/T_i and u'.

Keeping in mind these couplings, multilinear regressions of R/L_{n_C} are performed against five variables. The regressed $R/L_{n_C}^{reg}$ is of the form:

$$\left(\frac{R}{L_{n_C}}\right)^{reg} = \sum_{i=1}^{5} b_i x_i + constant \qquad (1)$$

with x_i the i^{th} variable and b_i its associated linear coefficient. For each coefficient, the uncertainty δb and statistical significance $b/\delta b$ (see [24] for more details) is computed. Regressions of R/L_{n_C} are performed for all combinations of 5 variables selected in the list of variables (mentioned above) and sorted as a function of the quality of the fit (standard deviation σ).

	b_1	b_2	δb_1	δb_2	STS_1	STS_2
u'	-1.94	-2.95	0.64	0.708	3.1	4.2
R/L_n	0.702	0.89	0.233	0.22	3	4.1
M_D	11.6	18.7	5.9	6.1	2	3.1
$\hat{s}$	-1.04	-2.06	0.914	0.88	1.1	2.4
R/L_{T_e}	-0.05	-0.16	0.24	0.23	0.22	0.67
constant	-2.06	-1.47	2.16	2.25	0.95	0.65

TABLE I: Variables used in multilinear regression of Fig. 2 together with their corresponding linear coefficients b, uncertainty δb and statistical significance STS. The subscripts 1 and 2 correspond to the regression without and with additional weight on extremal values of R/L_{n_C} respectively.

		u'	R/L_n	R/L_{T_i}	R/L_{T_e}	β	ρ_*	$\hat{s}$	q	ν_*	T_e/T_i	M_D
$r/a = 0.35$	Occurences	**8**	**10**	3	5	2	1	2	**10**	2	1	6
	STS	**1.45**	**2.48**	1	0.05	0.3	0.16	0.34	**1.74**	0.32	0.03	1.35
$r/a = 0.45$	Occurences	4	**10**	**8**	10	2	3	6	4	1	1	1
	STS	1.63	**3**	**2.27**	0.7	0.74	1	1.6	1.5	0.65	0.83	1.55
$r/a = 0.55$	Occurences	**10**	**10**	1	7	1	0	5	4	1	3	**8**
	STS	**2.8**	**2.6**	0.33	0.4	0.34	_	1.34	1.14	0.37	0.75	**1.72**
$r/a = 0.65$	Occurences	4	3	1	5	6	**8**	2	**9**	1	5	6
	STS	1.11	0.66	0.49	0.96	1.18	**1.77**	0.52	**1.1**	0.97	1.28	1.5
$r/a = 0.75$	Occurences	**10**	**7**	**10**	1	2	4	**10**	2	1	1	2
	STS	**3.34**	**1.2**	**1.34**	0.2	0.35	0.75	**1.85**	0.25	0.23	0.17	0.16
$r/a = 0.85$	Occurences	**10**	**10**	2	**10**	2	4	3	3	2	4	0
	STS	**2.37**	**2**	0.64	**2.14**	0.61	0.73	0.57	0.66	0.45	0.7	_

TABLE II: Occurences of the variables used in the 10 best multilinear regressions for several radial locations. The mean statistical significance (STS) is also shown. Occurences above 6 and STS above 1 are highlighted in bold.

In Fig. 2, the best fit ($\sigma = 1.19$) is shown for $r/a = 0.55$ (blue squares). The linear trend due to extremal values of R/L_{n_C} is not recovered and only a trend from $-4 < R/L_{n_C} < 1$ is found. To account for these extremal values, their weight have been artificially increased. While the general trend is now captured by this regression, the quality of this fit is reduced ($\sigma = 1.43$). The variables used for the regressions, their linear coefficients b, uncertainty δb and statistical significance are shown in Table I. The most important parameters with respect to their statistical significance are u', R/L_n and M_D. The negative coefficient corresponding to u' suggests an outward convection associated to this parameter, but as noted before, R/L_{T_i} and u' are strongly coupled in these discharges. Furthermore, the regression with artificial additional weights yield the same qualitative results with an increased coefficient for u' which could indicate a strengthened role of outward convection.

Due to the correlations between plasma parameters, one can obtain several regressions which present similar σ but with different variables. To take into account the fact that several fits of equivalent quality exist, the 10

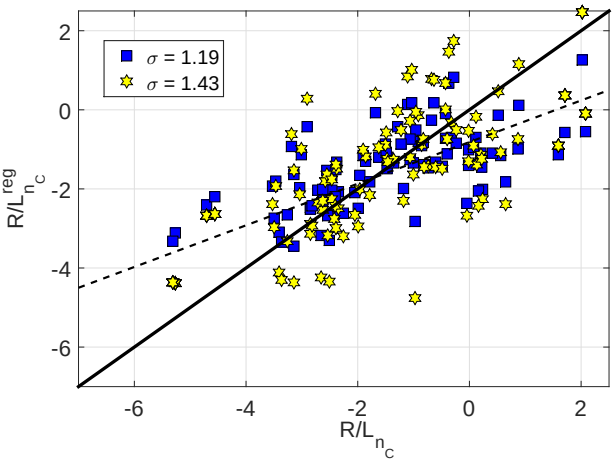

FIG. 2: Regressed versus experimental carbon peaking factor at $r/a = 0.55$. Regressions with (yellow hexagrams) / without (blue squares) artificially increased weigths for $R/L_{n_C} < -4$ and $R/L_{n_C} > 1$ have been performed. The identity relation is shown with a full line and the linear trend of the regression (blue squares) is highlighted by a dashed line. Parameters used in these regressions are gathered in Table I

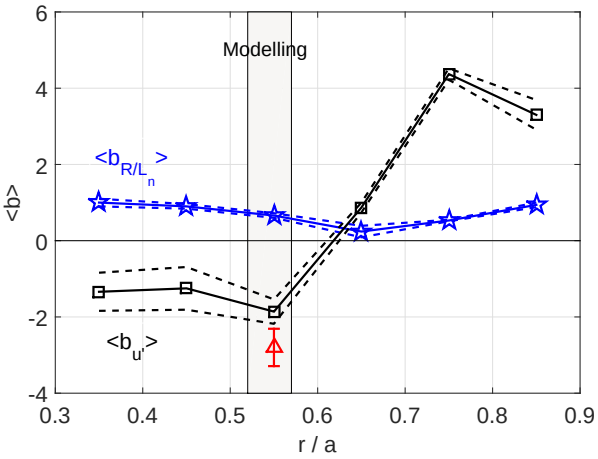

FIG. 3: Mean coefficient $< b >$ for u' and R/L_n described in the text versus r/a. The standard deviation of $< b >$ is also shown with dotted lines. The radial domain where simulations are performed is highlighted. The mean coefficient for u' found in the regression with increased weight is also shown (red triangle).

best results are gathered in Table II. The number of occurences of each variables is indicated, together with their mean statistical significance (computed from the 10 regressions), and the regressions are extended to the radial domain $r/a = 0.35 - 0.85$.

With respect to the occurences, the best parameters to fit R/L_{n_C} at $r/a = 0.55$ are u', R/L_n and M_D. The higher number of occurences of u' compared to R/L_{T_i} could come from their correlation and can not be interpreted as a weaker importance of R/L_{T_i}. For outter radii, R/L_{T_e} and $\hat{s}$ become dominant parameters with u' and R/L_n. This suggests an increasing role of electron turbulence such as trapped electron modes (dependent on $\hat{s}$) or electron temperature gradient modes (dependent on R/L_{T_e}) in the impurity transport channel but is not adressed in this study. Finally, u' and R/L_n are observed to be important parameters for the whole radial domain.

From these 10 best fits, one can then derive a mean linear coefficient for the variables u' and R/L_n at each radial position. This leads to Fig. 3 where the mean coefficients $< b >$ together with their standard deviation are shown versus the normalised minor radius.

In the core, the negative values of $< b >$ for u' again suggest an outward convection proportional to u' which flattens the profiles ($R/L_{n_C} \leq 0$). On the contrary, at the edge $< b >$ is positive which now suggests an inward convection (peaked profiles, i.e. positive R/L_{n_C}). These observations seem to be consistent with typical carbon profiles of Fig. 1 with respect to the direction of the convective mechanism associated to u'. On the other hand the coefficient related to R/L_n is rather constant throughout the radial domain. Also note that the standard deviation of the coefficient b in the 10 best fits is relatively small which underlines the consistency of such regressions with the u' and R/L_n parameters.

III. GYROKINETIC AND NEOCLASSICAL MODELLING METHODOLOGY

In this section, the modelling assumptions for the neoclassical and turbulent impurity transport are detailed. The total impurity flux is decomposed into a neoclassical and a turbulent component:

$$\Gamma_{tot} = \Gamma_{neo} + \Gamma_{turb} \tag{2}$$

The neoclassical transport is computed using the code NEO and the turbulent transport using the gyrokinetic code GKW. The latter is first adressed and the contributions of the neoclassical transport on the total carbon peaking factor are then considered. Mechanisms such as the impact of the neoclassical background on turbulent impurity transport [26] has been tested and found negligible for carbon transport in this database. Possible additional synergies between neoclassical and turbulent impurity transport are not considered in this study.

A. Gyrokinetic modelling methodology

In all the following linear simulations, the local assumption is employed and justified ($\rho_* \sim 1/500$ at mid-radius). Parallel perturbations of the potential $\delta A_\parallel$ are kept but not the perpendicular component $\delta A_\perp$. The latter has been found to have negligible effect on impurity transport modelling for this database, although the normalised electron pressure $\beta_e = 2\mu_0 n_e T_e / B^2$ can reach values up to 1%. Collisions are modelled via the pitch-angle scattering operator together with an ad-hoc momentum restoring term (the effect of energy scattering is marginal for these ITG cases [27]). Due to the presence of strong NBI in this database and hence strong toroidal rotation and its associated gradient, centrifugal and Coriolis drifts are taken into account. Finally the

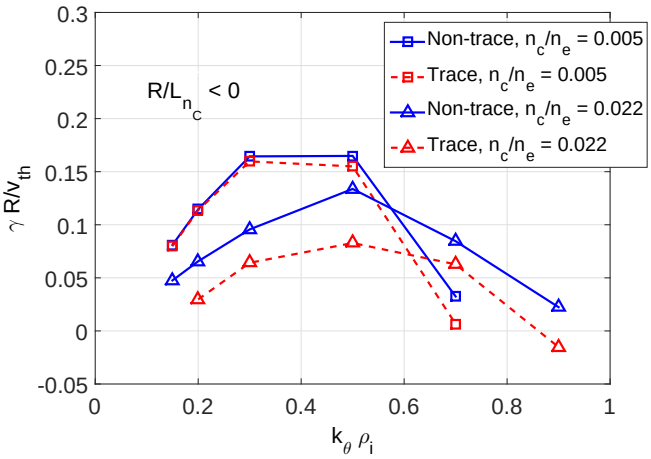

FIG. 4: Normalised growth rate versus the normalised poloidal wave number for a low (squares) and medium (triangles) carbon density case at $r/a = 0.55$. The trace assumption (dotted lines) is compared to the non-trace decomposition (full lines) used in this work.

experimental magnetic field geometry, computed from EFIT, is used. In specific cases where sensitivity tests are performed on the magnetic shear and safety factor, the Miller parametrisation of the flux surfaces is also employed [29].

After convergence tests, the following numerical grids are selected: $n_\mu = 12$, $n_{v_\parallel} = 64$, $n_s/n_{pt} = 32$ and $n_{pt} = 13$ for the number of points in the magnetic moment, parallel velocity, parallel direction, and the number of poloidal turns respectively. In Fig. 4, growth rate spectra are shown for cases with low and medium experimental carbon concentrations. The trace and non-trace simulations are compared. It is shown that at low concentration ($n_c/n_e = 0.005$), the two assumptions converge. On the other hand for a medium (for this database) carbon concentration ($n_c/n_e = 0.022$), the ion temperature gradient instability is destabilised by the presence of impurities. This is due to the negative carbon peaking factor at this radial location and has been described in [40, 41]. In the following, carbon is not considered as a trace in the simulations (concentrations up to 4%) and the experimental density and gradients values are kept.

To adress the large number of entries in the database and build a statistically relevant comparison between experiment and modelling, a quasi-linear approach is adopted [30–33]. This approach is based on the assumption that the characteristic turbulent diffusivity scales as:

$$D = \frac{\gamma}{< k_\perp^2 >} \tag{3}$$

with γ the most unstable linear growth rate and $k_\perp$ the perpendicular wave vector. This makes use of a characteristic time scale $\Delta t = 1/\gamma$ and a characteristic length scale $(\Delta x)^2 = 1/ < k_\perp^2 >$ given by:

$$< k_\perp^2 >= \frac{\int |\phi|^2 k_\perp^2 \mathrm{d}s}{\int |\phi|^2 \mathrm{d}s} \tag{4}$$

which takes into account the extended structure of the electrostatic potential ϕ along the field line. In normalised units the impurity flux can then be written as:

$$\Gamma_{QL} = \sum_{k_\theta} \Gamma_{k_\theta} \frac{\gamma_{k_\theta}}{< k_\perp^2 >} \tag{5}$$

where Γ_{k_θ} is the flux surface averaged linear impurity flux for a given k_θ and normalised with the corresponding value of $< |\phi|^2 >$. By default, the quasi-linear flux is assessed at $k_r \rho_i = 0$, but one could build more complex quasi-linear models including finite k_r contributions, see e.g. [38]. This flux can be further decomposed into a diffusive and a convective part:

$$\Gamma_{QL} = \frac{n}{R} D_{QL} \left(\frac{R}{L_n} + C_{T,QL} \frac{R}{L_T} + C_{u,QL} u' + C_{p,QL} \right) \tag{6}$$

with D_{QL}, $C_{T,QL}$, $C_{u,QL}$ and $C_{p,QL}$ the quasilinear diffusivity, thermo-diffusion coefficient, roto-diffusion coefficient and constant pinch respectively. These are directly linked to the diffusive and convective coefficients of each spectral component Γ_{k_θ} of the total quasi-linear flux Γ_{QL}:

$$D_{QL} = \sum_{k_\theta} D_{k_\theta} \frac{\gamma_{k_\theta}}{< k_\perp^2 >} \tag{7}$$

$$C_{p,QL} = \sum_{k_\theta} D_{k_\theta} C_{p,k_\theta} \frac{\gamma_{k_\theta}}{< k_\perp^2 >} / D_{QL} \tag{8}$$

$$C_{T,QL} = \sum_{k_\theta} D_{k_\theta} C_{T,k_\theta} \frac{\gamma_{k_\theta}}{< k_\perp^2 >} / D_{QL} \tag{9}$$

$$C_{u,QL} = \sum_{k_\theta} D_{k_\theta} C_{u,k_\theta} \frac{\gamma_{k_\theta}}{< k_\perp^2 >} / D_{QL} \tag{10}$$

$$\tag{11}$$

In steady state and without carbon sources, the carbon peaking factor then directly follows:

$$\frac{R}{L_{nC}} = -C_{p,QL} - C_{T,QL} \frac{R}{L_T} - C_{u,QL} u' \tag{12}$$

To separatly evaluate the transport coefficients, four impurities are used in the simulations with different normalised gradients (similarly to [39]). The combination of these impurities is strictly equivalent to having one impurity species with experimental levels of concentration and gradients.

In all the subsequent quasi-linear estimates, the spectral range $k_\theta \rho_i = [0.15; 0.2; 0.3; 0.5; 0.7; 0.9]$ and $k_r \rho_i = 0$ have been used. As the carbon peaking factor only depends on fluxes ratio, it is not sensitive to the saturation

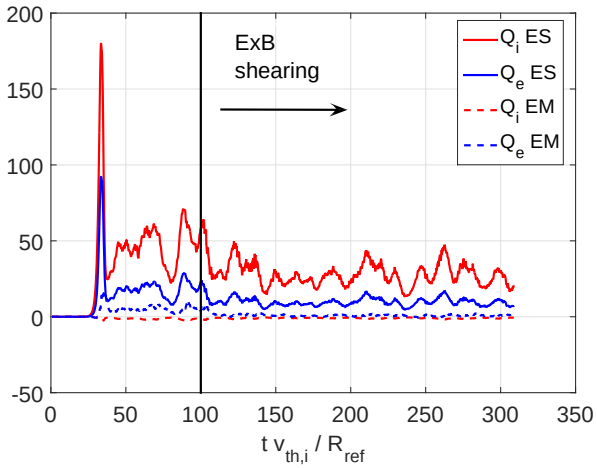

FIG. 5: Time traces of the normalised non-linear electron and ion heat fluxes. Electrostatic/electromagnetic contributions to the fluxes are shown in solid/dashed lines. $E \times B$ shearing is added to the simulation at the normalised time $tv_{th,i}/R_{ref} = 100$.

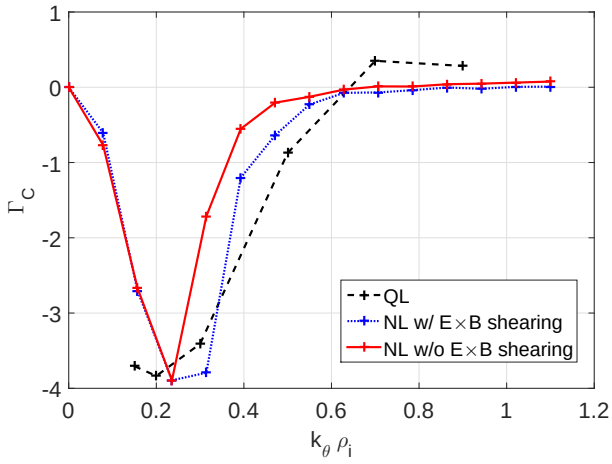

FIG. 6: Quasi-linear and non-linear spectra of the normalised carbon flux in $k_\theta \rho_i$. The spectra have been rescaled in order to compare the shape and not the saturation.

amplitude and is only a function of the spectral shape in $k_\theta \rho_i$. This makes the quasi-linear approach particularly suited to address the prediction of impurity peaking (the major difficulty of quasi-linear models is to predict the non-linear saturation level).

The size of the spectral range has also been extended to electron scales $k_\theta \rho_i = 40$, keeping the same mixing length rule for testing purposes. This yields a large electron heat flux generated by the Electron Temperature Gradient driven mode but also a non-zero impurity flux. The latter contributes to a significant increase of R/L_{n_C} due to an increased inward convection (electron turbulence). Nevertheless, the experimental ratio Q_i/Q_e is greatly underestimated due to the large Q_e generated at electon scales and using the mixing length of Eq. 3 which suggests that the impact of small scales turbulence on R/L_{n_C} should be evaluated with a proper weighting of these scales.

A non-linear simulation has also been performed to validate the quasi-linear approach and quantitatively investigate non-linear mechanisms responsible for light impurity transport. The following gridsizes have been used: $n_\mu = 16$, $n_{v_\parallel} = 50$, $n_s/n_{pt} = 32$, 339 radial wave vectors, 15 binormal wave vectors with $k_\theta \rho_i$ ranging from 0 to 1.1 and $k_r \rho_i$ ranging from -21 to $+21$. To evaluate the impact of $E \times B$ shearing, two non-linear simulations have been performed with and without this mechanism.

Time traces of the non-linear simulation with $E \times B$ shearing is shown in Fig. 5 and a comparison with the quasi-linear spectrum of the carbon flux is performed in Fig. 6. Electromagnetic contributions to the electron and ion heat fluxes are found to be negligible compared to the electrostatic part, although $\beta_e = 1\%$. The effect of $E \times B$ shearing is significant ($u' = 1.55$) and reduce the saturation amplitude of the non-linear heat fluxes as expected.

The quasi-linear carbon flux spectrum, after rescaling its amplitude (which has no effect on the carbon peaking factor modelling as stated above), is found to peak roughly at the same poloidal wave number than the corresponding non-linear spectrum (also rescaled) without $E \times B$ shearing (summed over the $k_r \rho_i$). Contributions at higher poloidal wave numbers are overestimated in the quasi-linear estimate (for this case). It can also be shown that the non-linear carbon flux summed over the poloidal wave numbers, peaks at $k_r \rho_i = 0$ which justifies the choice made for the quasi-linear approach. Nevertheless, this assumption will also be tested in section IV where the quasi-linear peaking factor is evaluated for nonzero $k_r \rho_i$.

B. Neoclassical contributions

To account for the neoclassical contributions in the modelling of R/L_{n_C}, the same methodology as in [2] is used. The quasi-linear turbulent fluxes are rescaled so that they match the experimental heat fluxes Q^{exp}:

$$\Gamma_C = \Gamma_{C,neo} + \Gamma^{QL}_{C,turb} \frac{Q_i^{exp} - Q_i^{neo}}{Q_i^{QL}} \tag{13}$$

For a zero total carbon flux (stationary phase and no carbon sources in the core), this equation yields the following expression of the peaking factor:

$$\frac{R}{L_{n_C}} = -\frac{RV^{QL}/\chi_i^{QL} + RV^{neo}/\chi_i^{an}}{D^{QL}/\chi_i^{QL} + D^{neo}/\chi_i^{an}} \tag{14}$$

where

$$V^{QL} = D^{QL} \left(C_{T,QL} \frac{R}{L_T} + C_{u,QL} u' + C_{p,QL} \right) \tag{15}$$

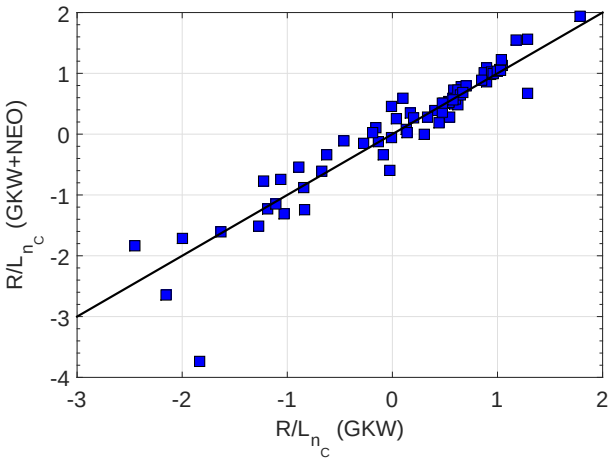

FIG. 7: Turbulent and neoclassical carbon peaking factor computed from GKW and NEO compared to turbulent R/L_{n_C} only.

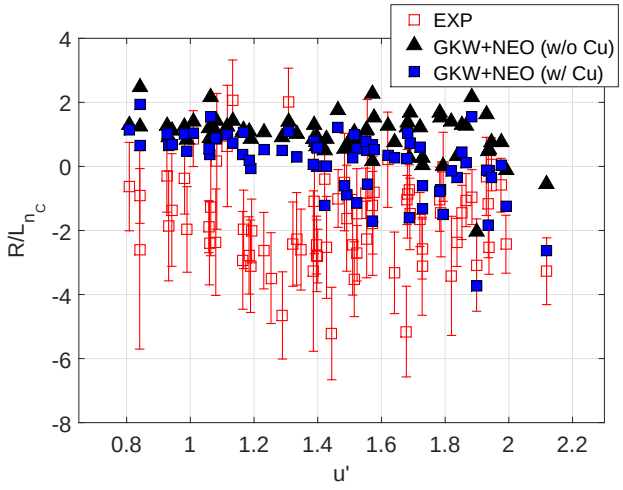

FIG. 8: Carbon peaking factor at $r/a = 0.55$ versus the normalised toroidal rotation gradient u'. Modelling results are shown with/without roto-diffusion and compared to the experimental values.

The super/subscripts *neo* and QL stand for neoclassical and turbulent quantities. χ_i^{an} and χ_i^{QL} are the anomalous and quasi-linear heat diffusivities respectively, computed from $Q_i^{exp} - Q_i^{neo}$ for the former and Q_i^{QL} for the latter, using the relation $Q_i = (n_i T_i/R)\chi_i R/L_{T_i}$.

In Fig. 7 the carbon peaking factor computed from Eq. 14 is compared to the turbulent R/L_{n_C} computed from Eq. 12. It is shown that for positive predicted values of R/L_{n_C}, neoclassical contributions are negligible. On the other hand for values of R/L_{n_C} close to zero or for negative values, neoclassical contributions are not negligible and should be taken into account to attempt quantitative comparisons with the experiment. From now on the modelled peaking factor always takes into account the neoclassical contributions.

IV. EXPERIMENT VS SIMULATIONS

In this section, the simulations focus at $r/a = 0.55$, where the carbon profiles are experimentally very hollow. For two particular cases the comparison is extended to the radial domain $r/a = 0.45 - 0.85$.

A. Experimental and modelled R/L_{n_C} at $r/a = 0.55$

To underline the importance of roto-diffusion on light impurity transport, the modelled carbon peaking factor is plotted versus the normalised toroidal rotation gradient u' and compared to corresponding experimental values in Fig. 8. It is to be noted that in these simulations, ITG turbulence is dominant which gives outward contributions for thermo-diffusion C_T and roto-diffusion C_u and an inward contribution for the curvature pinch C_p, as predicted by theory [1].

Including the roto-diffusion term in the modelling of R/L_{n_C} yields flatter and even hollow profiles for sufficiently large values of u'. This result goes in the same direction as found in AUG [2, 3], i.e. outward roto-diffusion plays a quantitatively important role in establishing the light impurity peaking factor going from positive to negative values. Although this effect is quite strong in reversing the sign of the peaking factor, most experimental values lie below the modelled R/L_{n_C} by a significant amount.

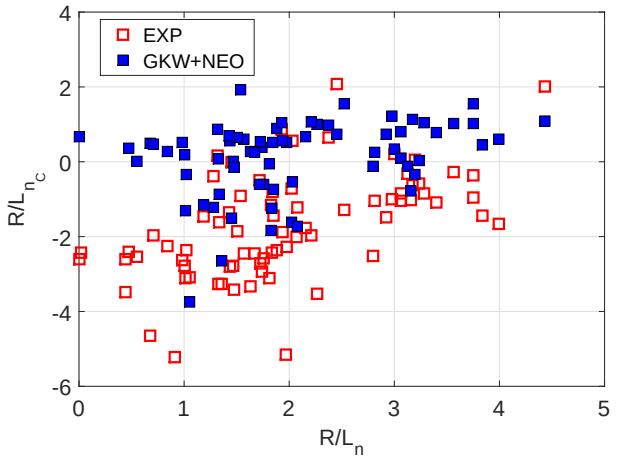

FIG. 9: Carbon peaking factor versus R/L_n at $r/a = 0.55$. Experimental error bars have been omitted for clarity.

As we have seen in the multilinear regressions of section II, R/L_{n_C} is strongly connected to R/L_n. In Fig. 9, comparisons between modelled and experimental R/L_{n_C} are shown versus R/L_n. The discrepancy between theory and experiment is observed over the whole R/L_n domain. Therefore, there is no clear correlation between the theoretical and experimental mismatch and R/L_n, or in other words, the experimental correlation observed between R/L_{n_C} and R/L_n is partly recovered in the modelling.

After extensive analysis of the disagreement between

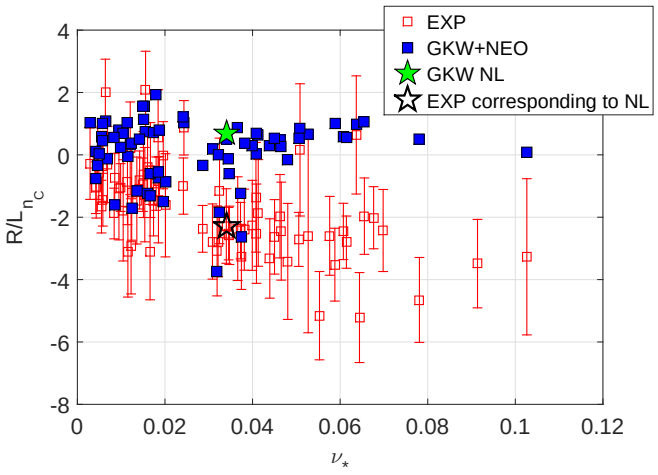

FIG. 10: Carbon peaking factor versus the normalised collisionality ν_*. Modelling results using the quasi-linear approach are compared to the experimental values. The result of a non-linear simulation is also shown, where the disagreement between the experimental and modelled value is substantial.

theoretical and experimental R/L_{n_C} in the parameter space, the modelled and experimental peaking factor are shown versus the normalised collisionality ν_* in Fig. 10, which is correlated to R/L_n and T_e/T_i. The ν_* dependency unravels two different regimes. At low ν_*, the agreement between modelling and experiment is satisfactory, within the experimental error bars. On the other hand, at higher ν_*, the disagreement is systematic and while the predictions are peaked (positive R/L_{n_C}), the experimental profiles are significantly hollow (negative R/L_{n_C}). A non-linear simulation, presentend in section III and performed where the disagreement between theory and experiment is substantial ($R/L_{n_C}^{exp} = -2.1$, $R/L_{n_C}^{QL} = 0.6$), for the parameters of Tab. III, confirms the validity of the quasi-linear approach: the non-linear peaking factor $R/L_{n_C} = 0.7$ is almost identical to the quasi-linear estimate. $E \times B$ shearing impacts the roto-diffusion coefficient due to symmetry breaking but also modifies the curvature pinch and thermo-diffusion, yielding a marginal change in R/L_{n_C} (0.72) for this case. This suggests that the quasi-linear approach is satisfactory in this domain of parameters and that the discrepancy observed with the experiment does not come from non-linear mechanisms such as $E \times B$ shearing or subdominant modes. However this does not rule out possible missing ingredients related to non-linear physics. Finally the same conclusions can be drawn when comparing the experimental and predicted values of R/L_{n_C} versus T_e/T_i due the strong correlation with ν_* (see Table V). At $T_e/T_i < 1$, theory and experiment are in good agreement whereas for $T_e/T_i > 1$, a systematic disagreement occurs.

Several sensitivity tests have been performed for a case at $\nu_* = 0.06$ to assess the role of important parameters such as the magnetic shear and safety factor in the discrepancy observed. The predicted R/L_{n_C} for this case is 1 whereas the experimental value is $R/L_{n_C}^{exp} = -3.5$.

$\hat{s}$	q	ϵ	T_e/T_i	R/L_{n_e}	R/L_{T_e}	R/L_{T_i}	u'	β	u	ν_*
1.01	1.57	0.17	1.186	1.98	4.62	6.78	1.55	1%	0.22	0.034

TABLE III: Input parameters for the non-linear simulation corresponding to shot number 68660 at t=9.2 s.

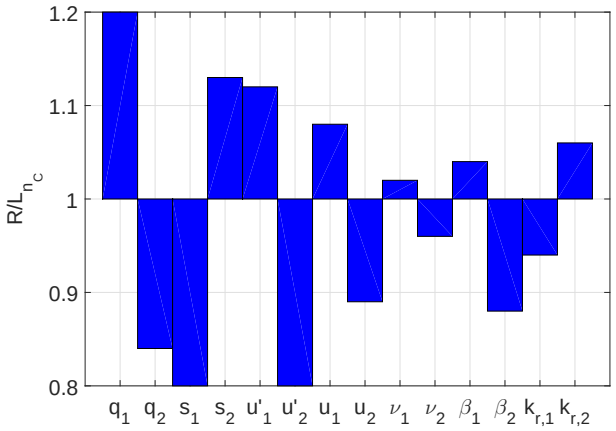

FIG. 11: Carbon peaking factor obtained for different values of the corresponding plasma parameters represented on the x-axis for the case at $\nu_* = 0.06$. The values of these parameters are gathered in Table IV and are varied around their nominal values.

These tests are shown in Fig. 11 together with the corresponding values of the plasma parameters in Table IV. The latter have been varied independently around their nominal values. The sensitivity of R/L_{n_C} with R/L_n, R/L_{T_i}, T_e/T_i and R/L_{T_e} not shown in Fig. 11 have also been checked yielding negligible modifications of the carbon peaking factor. All parameters have been consistently changed in NEO and GKW. The most sensitive parameters with respect to variations of the carbon peaking factor, are the safety factor as also shown in [3] and u'. Increasing these parameters flattens the predicted carbon profile as expected. Nonetheless, the values needed to recover the experimental R/L_{n_C} are far beyond the error bars. A sensitivity test has also been performed for the case in Table III, yielding the same results, that is, discrepancies between predicted and experimental values of R/L_{n_C} are robust with respect to variations of plasma parameters.

At this point, it is clear that an ingredient is missing in the modelling of the carbon peaking factor and this ingredient appears to be linked to the normalised collisionality ν_* (or T_e/T_i). The strong linear relation of the experimental peaking factor with u' found in section II, underlines a possible stronger outward convection mechanism than what is obtained in simulations. This improved convection should scale with ν_* (or T_e/T_i).

Parameter	β_1	β_2	q_1	q_2	$\hat{s}_1$	$\hat{s}_2$	u_1'	u_2'	u_1	u_2	$\nu_{*,1}$	$\nu_{*,2}$	$k_{r,1}\rho_i$	$k_{r,2}\rho_i$
Values of Fig.11	0.1%	0.5%	1.5	3.5	0.4	1.5	0.9	2.2	0.1	0.3	0.04	0.09	−0.1	0.1
Nominal values	0.26%		2.6		0.85		1.5		0.2		0.06		0	

TABLE IV: Values used for the sensitivity tests of Fig. 11. The nominal values are also listed.

B. Multi-channel analysis

To shed some light on the regime where experimental and theoretical R/L_{n_C} are in disagreement, the heat and momentum channels are scrutinised (Fig. 12). The problem of the turbulent saturation amplitude is set aside by looking at the ratio of the ion momentum flux to the ion heat flux (Π_i/Q_i) and the electron to ion heat flux ratio (Q_e/Q_i). Their experimental counterpart are computed from the steady state momentum and heat transport equations, considering the particle, torque and heat NBI/ICRH sources together with electron-ion equipartition and Ohmic heating. The experimental ion momentum flux is corrected from the momentum carried by the particle flux [15]. The radiated power at mid-radius is found negligible.

Considering only the NBI heated plasmas, the predicted and experimental Π_i/Q_i feature two opposite trends with ν_* (or T_e/T_i). At low ν_*, theory and experiment are converging whereas at higher ν_* they are diverging. These trends are less clear for plasmas with non-zero ICRH, especially for $0.04 < \nu_* < 0.07$. The non-linear Π_i/Q_i is $\sim 20\%$ lower than the quasi-linear estimate (but still ~ 3 times higher than the experimental value) and $E\times B$ shearing does not affect significantly Π_i/Q_i in this regime.

It is known that the momentum flux and impurity roto-diffusion both stem from parallel symmetry breaking mechanisms [1, 18]. This peculiarity could underline a common missing ingredient in the modelling, linked to parallel symmetry and thus preventing quantitative comparisons at high ν_* of the ion momentum flux and the carbon peaking factor alltogether.

In contrast, the predicted ratio Q_i/Q_e in Fig. 12(b) is shown to be systematically higher than the experimental ratio, which is consistent with low $k_\theta\rho_i$ computations. While no particular care has been given matching the experimental heat fluxes ratio (non trivial additional physics could be needed such as multi-scale interactions [34, 35] or non-linear fast ions stabilisation [36]), no link between the theoretical discrepancies and ν_* is observed for this channel which further suggests that the discrepancies in R/L_{n_C} and Π_i/Q_i are related to a missing symmetry breaking mechanism.

C. Carbon profiles at low and high collisionalities

To gain more insight on the two collisionality regimes underlined in the previous section, simulations are performed over a larger fraction of the radial domain for two particular cases, one at low ν_* (0.012) and one at higher ν_* (0.034) from Table III.

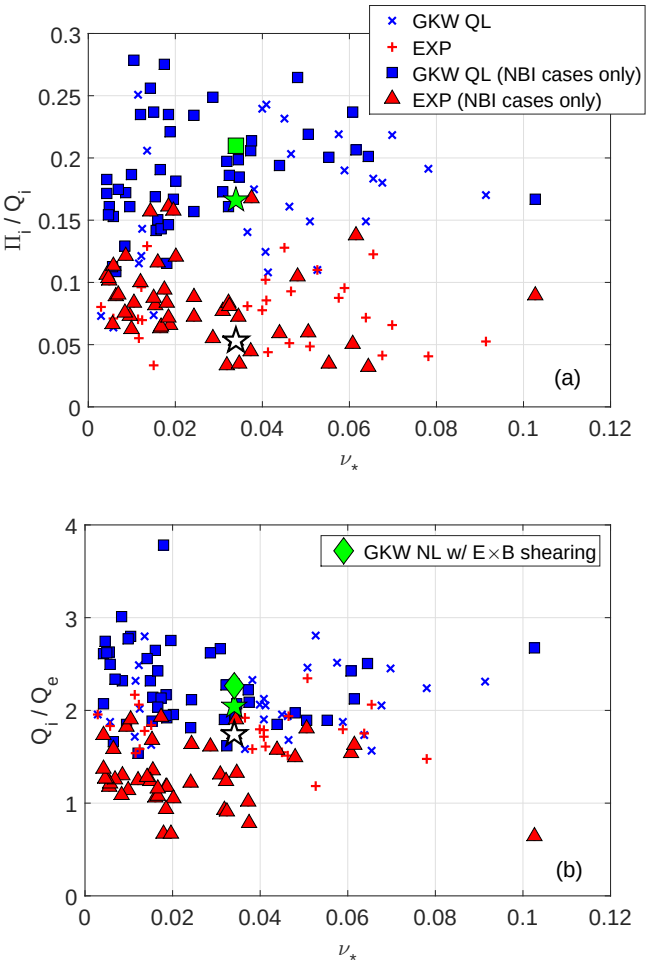

FIG. 12: Normalised ratio of the ion momentum flux with the ion heat flux (a) and the ion to electron heat flux ratio (b). Quasi-linear and non-linear (green pentagrams) values are compared with the experiment. The open pentagram and green square correspond to the experimental and predicted (quasi-linear) value respectively, associated to the non-linear simulation. The effect of $E\times B$ shearing is shown only for Q_i/Q_e where modifications of this ratio are visible (it also matches the associated quasi-linear value).

In Fig. 13 the predicted profiles of R/L_{n_C} are compared to the experimental one. Again modelled values with and without roto-diffusion are shown. For the low collisionality case (Fig. 13 (b)) the correspondence between prediction and experiment is strikingly accurate, provided roto-diffusion is taken into account, the latter being a critical ingredient for $r/a < 0.6$.

On the contrary, for the high collisionality case (Fig. 13 (a)), agreement between experiment and theory is very poor, except at one radial position where both pro-

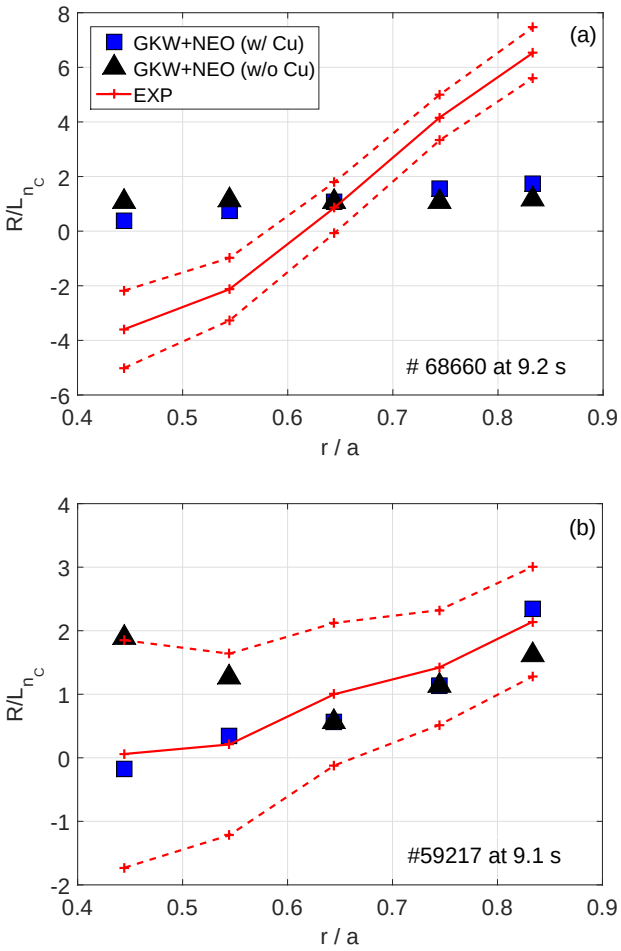

FIG. 13: Comparison of the carbon peaking factor profiles between fits from experimental carbon profiles and modelled values with/without roto-diffusion. Two particular cases are shown, at high (a) and low (b) ν_* with respect to Fig. 10.

files ultimately cross each other, the experimental profile showing strong radial variation from $R/L_{n_C} \sim -4$ to $R/L_{n_C} \sim 6$ at the edge. Roto-diffusion does not significantly affect the predictions in this case but tends to flatten/peak the carbon profile in the core/edge. The impact of roto-diffusion at the edge (in both collisionality cases) is due to a change in the turbulent drive going from a temperature gradient driven mode to a density gradient driven mode. Discrepancies at inner (hollow profile) and outter (peaked profile) radii could stem from very different physical mechanisms but could also have a similar effect (enhancement) on roto-diffusion as we have seen a strong correlation of the carbon peaking factor with u' over the whole radial domain in section II.

These results demonstrate the relevance of the standard modelling approach adopted but also shows that there are limitations where it is incomplete and requires additional, yet unknown, physical ingredients linked to the collisionality (or T_e/T_i). This should motivate further studies on high collisionality cases to identify the physics behind such experimental variations of R/L_{n_C}.

V. CONCLUSIONS

A database of H-modes in JET-C, extensively used to study momentum and particle transport properties in the past is scrutinised in this work for carbon transport. These discharges feature very hollow carbon density profiles with peaking factors (R/L_{n_C}) up to -5 at mid-radius and peaked at the plasma edge. These profile shapes are very favorable in terms of impurity accumulation avoidance which motivated a thourough study and understanding of the carbon transport in these plasmas.

To do so, gyrokinetic and neoclassical simulations are performed for a large number of database entries at mid-radius. To tackle the large number of simulations required, a quasi-linear approach is adopted and supported by non-linear simulations. Neoclassical transport of carbon is shown to be non-negligible compared to the quasi-linear turbulent transport. Therefore, comparisons between theoretical and experimental values of R/L_{n_C} are performed using the turbulent and neoclassical contributions. Two important results arise from this comparison and are divided in two regimes, at low and high normalised collisionality ν_* or at $T_e/T_i < 1$ and $T_e/T_i > 1$ respectively (these two parameters being strongly correlated in this database).

At low ν_*, the agreement between the theory and the experiment is satisfactory, provided roto-diffusion is taken into account. The latter provides an additional outward convection (together with thermo-diffusion) that is substantial in these NBI heated plasmas and confirms previous results on the importance of this mechanism [2, 3].

In contrast, at high ν_* the agreement is systematically poor. This is also confirmed by non-linear simulations and extensive sensitivity tests of the modelled result with variations of the input plasma parameters. The effect of non-linear $E\times B$ shearing is found negligible and does not fill the gap between predicted and experimental R/L_{n_C}.

A multi-channel analysis has been performed, i.e. comparisons of the experimental and modelled ratios of ion momentum flux to ion heat flux (Π_i/Q_i) and ion to electron heat fluxes (Q_i/Q_e). Π_i/Q_i features two collisionality regimes when compared to the experiment, similarly to the carbon peaking factor. On the other hand discrepancies between experimental and theoretical Q_i/Q_e are found to be independent of the normalised collisionality ν_*. The similar disagreement for the ion momentum flux and R/L_{n_C} could hint toward a common missing ingredient linked to parallel symmetry breaking mechanisms and ν_*.

Finally comparisons of the theoretical and experimental R/L_{n_C} are performed over a large fraction of the minor radius $r/a = 0.45-0.85$ for a low and high collisionality cases. At low ν_*, the agreement is very good over the whole radial domain while at high ν_*, the experimental R/L_{n_C} features strong radial variations which are not captured by the modelling. At mid-radius, the experimental carbon peaking factor is over-estimated while at $r/a \sim 0.8$, it is under-estimated. The strong experimental hollowness (also observed at ASDEX Upgrade [37])

in the core and peaking at the edge could stem from different physical mechanisms. Further studies are needed to identify the mechanisms currently missing in the light impurity transport modelling paradigm.

Acknowledgments

The authors acknowledge very fruitful discussions with A. Kappatou, R. McDermott, N. Bonanomi, and P. Mantica. Part of this work was performed using HPC resources from GENCI-IDRIS (Grant No. 2014-056892). Part of this work was granted access to the HPC resources of Aix-Marseille Université financed by the project Equip@Meso (ANR-10-EQPX-29-01) of the program "Investissements d'Avenir" supervised by the Agence Nationale pour la Recherche. This work has been carried out within the framework EUROfusion Consortium and has received funding from the Euratom research and training programme 2014 − 2018 under grant agreement No 633053. The views and opinions expressed herein do not necessarily reflect those of the European Commission.

Appendix A: Correlation table at $r/a = 0.55$

To determine correlations in the database studied in this paper, the following definition of the correlation coefficient $r_c(y, z)$ between the variables y and z has been used:

$$r_c(y,z) = 1 - \frac{\sum_{i=1}^{N}(y_i - y_{fit,i})^2}{NV(y)} \tag{16}$$

with N the number of points in the database, y_i the i^{th} value of the considered variable y, $y_{fit}(z)$ the linear fit of y with respect to z ($y_{fit} = a\times z+b$) and $y_{fit,i} = a\times z_i+b$. $V(y)$ is the variance defined by:

$$V(y) = \frac{1}{N}\sum_{i=1}^{N}(y_i - m)^2 \tag{17}$$

with m the mean value of the y_i.

This definition of the correlation parameter yields a perfect correlation ($r_c = 1$) for $y_i = y_{fit,i}$ for each $i = 1$ to N and no correlation ($r_c = 0$) for $y_{fit} = m$. The latter condition is fullfilled when the slope of the linear function $y_{fit}(z)$ is zero. Table V gather these correlations for a set of physically relevant parameters: $u' = R^2\partial\Omega/\partial r/v_{th,i}$, R/L_n, R/L_{T_i}, R/L_{T_e}, the ratio of the total plasma pressure to magnetic pressure β, $\rho_* = \rho_i/a$ with a the plasma minor radius at the last closed flux surface, the safety factor q, the magnetic shear $\hat{s}$, the normalised collisionality $\nu_* = \nu_{ei}q/\epsilon^{3/2}$,$T_e/T_i$,$M_D$ and R/L_{n_C}. Correlations below $r_c = 0.05$ are set to zero and are not discussed.

	u'	R/L_n	R/L_{T_i}	R/L_{T_e}	β	ρ_*	$\hat{s}$	q	ν_*	T_e/T_i	M_D	R/L_{n_C}
u'	1	0.08	**0.36**	0	0.07	0.14	0	0	0	0	0.14	0.06
R/L_n	0.08	1	0	0	0	0	0	0	**0.5**	0.19	0	0.13
R/L_{T_i}	**0.36**	0	1	0	0	0.13	0	0	0	0	0	0
R/L_{T_e}	0	0	0	1	0.1	0.15	0	0.06	0.07	0.1	0.17	0
β	0.07	0	0	0.1	1	**0.6**	0	**0.44**	0.12	0.2	**0.31**	0
ρ_*	0.14	0	0.13	0.15	**0.6**	1	0	**0.27**	**0.42**	**0.29**	0.23	0
$\hat{s}$	0	0	0	0	0	0	1	0	0	0	0	0
q	0	0	0	0.06	**0.44**	**0.27**	0	1	0.16	0.17	0.13	0.09
ν_*	0	**0.5**	0	0.07	0.12	**0.42**	0	0.16	1	**0.72**	0.2	0.16
T_e/T_i	0	0.19	0	0.1	0.2	**0.29**	0	0.17	**0.72**	1	**0.4**	0.17
M_D	0.14	0	0	0.17	**0.31**	0.23	0	0.13	0.2	**0.4**	1	0
R/L_{n_C}	0.06	0.13	0	0	0	0	0	0.09	0.16	0.17	0	1

TABLE V: Correlation table at $r/a = 0.55$ using Eq. 16. Values above 0.2 are highlighted in bold.

[1] C. Angioni, Y. Camenen, F. J. Casson, E. Fable, R. M. McDermott, A. G. Peeters and J. E. Rice, Nuclear Fusion **52**, 114003 (2012)

[2] C. Angioni, R. M. McDermott, E. Fable, R. Fischer, T. Pütterich, F. Ryter, G. Tardini and the ASDEX Upgrade Team, Nuclear Fusion, **51**, 023006 (2011)

[3] F. J. Casson, R. M. McDermott, C. Angioni, Y. Camenen, R. Dux, E. Fable, R. Fischer, B. Geiger, P. Manas,

L. Menchero, G. Tardini and the ASDEX Upgrade Team, Nuclear Fusion **53**, 063026 (2013)
[4] H. Nordman, A. Skyman, P. Strand, C. Giroud, F. Jenko, F. Merz, V. Naulin, T. Tala and the JET-EFDA Contributors, Plasmas Physics and Controlled Fusion **53**, 105005 (2011)
[5] A. Skyman, L. Fazendeiro, D. Tegnered, H. Nordman, J. ANderson and P. Strand, Nuclear Fusion **54**, 013009 (2013)
[6] D. R. Mikkelsen *et al*, Physics of Plasmas **22**, 062301 (2015)
[7] D. R. Mikkelsen *et al*, Physics of Plasmas **21**, 082302 (2014)
[8] A. Kappatou, PhD thesis, Eindhoven University of Technology, the Netherlands (2014)
[9] A. Kappatou *et al*, 42$^{\text{nd}}$ EPS Conference on Plasma Physics (2015)
[10] M. R. Wade, W. A. Houlberg and L. R. Baylor, Physical Review Letters **84**, 282 (2000)
[11] N. T. Howard, M. Greenwald, D. R. Mikkelsen, M. L. Reinke, A. E. White, D. Ernst, Y. Podpaly and J. Candy, Nuclear Fusion **52**, 063002 (2012)
[12] C. Angioni *et al*, Nuclear Fusion **54**, 083028 (2014)
[13] F. J. Casson *et al*, Plasma Physics and Controlled Fusion **57**, 014031 (2015)
[14] M. Maslov, C. Angioni, H. Weisen and JET-EFDA contributors, Nuclear Fusion **49**, 075037 (2009)
[15] H. Weisen, Y. Camenen, A. Salmi, T. W. Versloot, P. C. de Vries, M. Maslov, T. Tala, M. Beurskens, C. Giroud and JET-EFDA contributors, Nuclear Fusion **52**, 042001 (2012)
[16] H. Weisen, Y. Camenen, A. Salmi, T. W. Versloot, P. C. de Vries, M. Maslov, T. Tala, M. Beurskens, C. Giroud and JET-EFDA contributors, Nuclear Fusion **52**, 114024 (2012)
[17] C. Angioni, A. G. Peeters, Physical Review Letters **96**, 095003 (2006)
[18] Y. Camenen, A. G. Peeters, C. Angioni, F. J. Casson, W. A. Hornsby, A. P. Snodin and D. Strintzi, Physics of Plasmas, **16**, 012503 (2009)
[19] E. A. Belli and J. Candy, Plasma Physics and Controlled Fusion **51**, 075018 (2009)
[20] A. G. Peeters, Y. Camenen, F. J. Casson, W. A. Hornsby, A. P. Snodin, D. Strintzi, G. Szepezi, Computer Physics Commnunications **180**, 2650 (2009)
[21] L. L. Lao, H. S. John, R. D. Stambaugh, A. G. Kellman and W. Pfeiffer, Nuclear Fusion **25**, 1611 (1985)
[22] C. Giroud *et al*, Review of Scientific Instruments **79**, 10F525 (2008)
[23] A. Bortolon, Y. Camenen, A. N. Karpushov, B. P. Duval, Y. Andrebe, L. Dederspiel, O. Sauter and the TCV Team, Nuclear Fusion **53**, 023002 (2013)
[24] C. Angioni *et al*, Nuclear Fusion **47**, 1326 (2007)
[25] C. Angioni, E. Fable, M. Greenwald, M. Maslov, A. G. Peeters, H. Takenaga and H. Weisen, Plasma Physics and Controlled Fusion **51**, 124017 (2009)
[26] P. Manas, W. A. Hornsby, C. Angioni, Y. Camenen and A. G. Peeters, *accepted in* Plasma Physics and Controlled Fusion
[27] P. Manas, Y. Camenen, S. Benkadda, W. A. Hornsby, and A. G. Peeters, Physics of Plasmas **22**, 062302 (2015)
[28] H. Lütjens, A. Bondeson, O. Sauter, Computer Physics Communication **97**, 219 (1996)
[29] R. L. Miller, M. S. Chu, J. M. Greene, Y. R. Lin-Liu and R. E. Waltz, Physics of Plasmas **5**, 973 (1998)
[30] F. Jenko, T. Dannert and C. Angioni, Plasma Physics and Controlled Fusion **47**/, B195 (2005)
[31] M. Kotschenreuther, W. Dorland, M. A. Beer and G. W. Hammett, Physics of Plasmas **2**, 2381 (1995)
[32] J. E. Kinsey, G. M. Staebler and R. E. Waltz, Physics of Plasmas **15**, 055908 (2008)
[33] A. Casati *et al*, Nuclear Fusion **49**, 085012 (2009)
[34] N. T. Howard, C. Holland, A. E. White, M. Greenwald and J. Candy, Nuclear Fusion **56**, 014004 (2016)
[35] S. Maeyama, Y. Idomura, T.-H. Watanabe, M. Nakata, M. Yagi, N. Miyato, A. Ishizawa and M. Nunami, Physical Review Letters **114**, 255002 (2015)
[36] J. Citrin, F. Jenko, P. Mantica, D. Told, C. Bourdelle, J. Garcia, J. W. Haverkort, G. M. D. Hogeweij, T. Johnson and M. J. Pueschel, Physical Review Letters **111**, 155001 (2013)
[37] M. N. A. Beurskens *et al*, Nuclear Fusion **56**, 056014 (2016)
[38] G. M. Staebler, R. E. Waltz, J. Candy, and J. E. Kinsey, Physical Review Letters **110**, 055003 (2013)
[39] C. Angioni, R. Dux, E. Fable, A. G. Peeters and the ASDEX Upgrade Team, Plasma Physics and Controlled Fusion **49**,2027 (2007)
[40] J. Q. Dong and W. Horton, Physics of Plasmas **2**, 3412 (1995)
[41] C. Estrada-Mila, J. Candy and R. E. Waltz, Physics of Plasmas **12**, 022305 (2005)